The nanoscale geometry of TiO$_2$ nanotubes influences the osteogenic differentiation of human adipose-derived stem cells by modulating H3K4 trimethylation

Longwei Lv [a,1], Yunsong Liu [a,1], Ping Zhang [a], Xiao Zhang [a], Jianzhang Liu [a], Tong Chen [a], Penglei Su [b], Hongyi Li [b,**], Yongsheng Zhou [a,c,*]

[a] Department of Prosthodontics, Peking University School and Hospital of Stomatology, Beijing 100081, China
[b] Photoelectrochemical Research Group, School of Materials Science and Engineering, Beijing University of Technology, Beijing 100124, China
[c] National Engineering Laboratory for Digital and Material Technology of Stomatology, Beijing 100081, China

ARTICLE INFO

ABSTRACT

Nanostructured materials can direct stem cell lineage commitment solely by their various, but controllable, geometric cues, which would be very important for their future application in bone tissue engineering and bone regeneration. However, the mechanisms by which nano-geometric cues dictate the osteogenic differentiation of stem cells remain unclear. Epigenetics is central to cellular differentiation, a process that regulates heritable and long-lasting alterations in gene expression without changing the DNA sequence. Here, we explored the varied osteogenic behaviors of human adipose-derived stem cells (hASCs) on titanium dioxide (TiO$_2$) nanotube arrays of different diameters. Both *in vitro* and *in vivo* studies demonstrated that the nanoscale geometry influenced cellular differentiation and TiO$_2$ nanotubes with a diameter of 70 nm was the optimal dimension for the osteogenic differentiation of hASCs. Moreover, we observed that TiO$_2$ nanotubes promoted the osteogenic differentiation of hASCs by upregulating methylation level of histone H3 at lysine 4 (H3K4) in the promoter regions of osteogenic genes Runx2 and osteocalcin, by inhibiting demethylase retinoblastoma binding protein 2 (RBP2). These results revealed, for the first time, the epigenetic mechanism by which nanotopography directs stem cell fate.

1. Introduction

Cell-nanotopography interactions are believed to represent a promising management to precisely control seed cell function and differentiation in bone tissue engineering, because bone itself has a structural hierarchy at the first level in the nanometer range [1–3]. Meanwhile, an increasing number of studies on various nano-structured materials, such as nanoscale pits [4,5], grooves [6,7] and nanofibers [8–10], have demonstrated their ability to regulate the osteogenic differentiation of mesenchymal stem cells. Among them, TiO$_2$ nanotube arrays, a kind of highly-ordered nanostructure with tunable geometric parameters, have shown promise for future clinical applications because it can be easily formed on the surface of either implants or three-dimensional scaffolds via facile anodic oxidation strategy [11], realizing osseointegration at both the 2D and 3D interfaces.

Moreover, TiO$_2$ nanotubes of different diameters can act as a new set of tools to study systematically the influence of nanoscale geometry on cell behaviors. Some early experiments proposed that a small tube diameter (e.g. 15–30 nm) could promote osteogenic differentiation of rat bone marrow derived mesenchymal stem cells (BMMSCs) by assisting cell adhesion [12,13]. Later, researchers found that a large tube diameter (e.g. 100 nm) benefited cell elongation, which might lead to a change in cytoskeletal stress, thus promoting osteogenic differentiation of human BMMSCs and mouse MC3T3 cells [14,15]. The latest *in vitro* and *in vivo* study proposed that there is an optimal medium tube diameter (e.g. 70 nm) for the osteogenic differentiation of mouse MC3T3 cells [16]

* Corresponding author. Department of Prosthodontics, Peking University School and Hospital of Stomatology, 22 Zhongguancun South Avenue, Haidian District, Beijing 100081, China. Tel.: +86 10 82195370 (office); fax: +86 10 62173402.
** Corresponding author. Tel./fax: +86 10 67391101.
E-mail addresses: lhy06@bjut.edu.cn (H. Li), kqzhouysh@hsc.pku.edu.cn (Y. Zhou).
[1] These authors contributed equally.

and implant osseointegration in minipigs [17]. However, until now, the optimal dimension of TiO$_2$ nanotubes for the osteogenic differentiation of human stem cells remains uncertain and the underlying mechanism of how nanoscale geometry influences cell differentiation needs to be clarified.

To answer the question of optimal dimension, more studies based on human cells and *in vivo* models are required, because cell species is likely to be an important factor in the variations among previous studies, and animal experiments to select the optimal dimension would be more convincing; however, there have been few of them.

In addition, some studies tried to explain the mechanism responsible for the favorable osteogenesis response to TiO$_2$ nanotubes in terms of protein adhesion or molecular signaling pathways [12,14]. Nevertheless, there is an important mechanism that seems to have been neglected. Epigenetic regulation of gene expression occurs via alterations in chromatin proteins that do not change the DNA sequence, through which process genes are switched on or off in a more durable fashion than other transient mechanisms of gene regulation, such as by transcription factors [18,19]. Thus, epigenetics is central to cellular differentiation and stem cell linage commitment. Geometric cues from material interfaces are crucial regulators of stem cell behavior and are important in tissue differentiation. However, there has been no demonstration of a mechanism whereby surface topography can affect gene regulation at the epigenetic level.

In this study, the effects of nanoscale geometry on cell differentiation were investigated *in vitro* and *in vivo* using human adipose-derived stem cells (hASCs) and TiO$_2$ nanotubes of three different diameters. Meanwhile, sandblasting with large grit and acid-etching (SLA) surface was chosen as a positive control due to its improved ability of osseointegration and its popularity in clinical application [20]. Furthermore, biochemical, molecular, and epigenetic approaches were utilized to screen how nanotopography directs stem cell fate.

2. Materials and methods

2.1. Preparation of titanium specimens

Titanium specimens were divided into three groups, including anodization groups (test groups), SLA group (positive control) and machined group (negative control). All pure titanium slices (99.6% purity, Leiden, Beijing, China) of three sizes, $10 \times 10 \times 0.2$ mm, $23 \times 23 \times 0.2$ mm (especially for RT-PCR, western blotting and ChIP assay), and $\phi 7$mm $\times$ 0.2 mm (especially for *in vivo* experiments) were polished with silicon carbide sandpaper of No. 240, 360, 400, 600, 800, 1000 and 2000 grits in series, and then washed with acetone, absolute alcohol and deionized water (dH$_2$O) (Milli-Q Ultra-Pure, Millipore, Billerica, MA, USA) in an ultrasonic cleaner, respectively, for 15min. Subsequently, the specimens were dried at room temperature for 1 h. The anodization and SLA groups were further processed as follows. TiO$_2$ nanotubes were obtained by anodization using graphite foil as counter cathode in an aqueous solution with 1 mol/L (NH$_4$)H$_2$PO$_4$ and 0.08 mol/L (NH$_4$)HF$_2$ under magnetic stirring with a constant speed at 20 °C for 2 h. The anodization voltages were 10 V, 20 V and 25 V, respectively. After being anodized, specimens were rinsed with distilled water three times and dried in air at 80 °C. Heat treatment was then performed at 450 °C for 2 h. For the SLA group, each titanium slice was sandblasted by 110 μm Al$_2$O$_3$ particles at a distance of 50 mm at an angle of 90°for 30 s. The air pressure used for sandblasting was set to 0.45 MPa. Subsequently, the specimens were etched using a mixture of 0.11 mol/L HF and 0.09 mol/L HNO$_3$, at room temperature for 10 min, and then in a mixture of 5.80 mol/L HCl and 8.96 mol/L H$_2$SO$_4$ at 60 °C for 30 min. The titanium specimens were cleaned ultrasonically in dH$_2$O for 15 min. All specimens were sterilized in an autoclave at 120 °C for 30 min for the *in vitro* experiments.

2.2. Surface characterization

The surface morphology of the TiO$_2$ nanotubes array thin films, SLA and machined smooth titanium surfaces were characterized using field emission scanning electron microscopy (FESEM; Hitachi, S4800, Tokyo, Japan). Atomic force microscopy (AFM, PI3800/SPA400, Seiko Instruments Inc, Tokyo, Japan) was used to investigate the surface morphology and surface roughness of the samples. Before AFM measurement, different samples were rinsed with ethanol and Milli-Q water, and dried in the air. The measurements were conducted under contact mode in dry conditions with a scan rate of 1 Hz, using a Si$_3$N$_4$ cantilever with a spring constant of 0.12 N/m (Seiko Instruments) for resolution imaging. The scan area was 20 μm $\times$ 20 μm. Measurements were run in triplicate for each sample. The crystalline phase of TiO$_2$ nanotube samples before and after heat treatment, as well as SLA and machined smooth titanium surfaces, were identified and analyzed by X-ray diffraction (XRD, AXS D8 Advanced, Germany) using a Cu target as the radiation source ($\lambda = 1.540598$ Å) at 40 kV. The diffraction angles (2θ) were set between 5° and 90°, incremented with a step size of 4°/min. Static contact angles and surface energy of both water and simulated body fluid (SBF) were measured by a SL200 contact angle system (Kino Industry, New York, NY, USA) at room temperature, and surface energy was calculated by the matching software from Kino Industry (http://www.uskino.com/article/65.html).

2.3. hASCs culture and osteogenic induction

hASCs were purchased from ScienCell Company (San Diego, CA, USA). This study was approved by the Ethics Committee of the Peking University Health Science Center, Beijing, China (PKUSSIRB-2013023). All materials were purchased from Sigma–Aldrich (St. Louis, MO, USA) unless otherwise stated. Dulbecco's modified Eagle's medium (DMEM), fetal bovine serum (FBS), 100× penicillin and streptomycin mixture were purchased from Gibco (Grand Island, NY, USA). hASCs were cultured in fresh DMEM containing 10% (v/v) FBS, 100 U/mL penicillin G and 100 mg/mL streptomycin at 37 °C in an incubator with an atmosphere consisting of 95% air, 5% CO$_2$ and 100% relative humidity. Cells at the fourth passage were used for the *in vitro* experiments and all *in vitro* experiments were repeated three times using hASCs from the three patients, respectively. Osteogenic inducing medium comprised fresh DMEM containing 10% (v/v) FBS, 100 U/mL penicillin G and 100 mg/mL streptomycin, 10 nM dexamethasone, 10 mM β-glycerophosphate and 50 μg/ml ʟ-ascorbic acid.

2.4. hASCs adhesion and proliferation assay

The proportional of cells adhering to sample surfaces were counted using CCK8 (Dojindo Laboratories, Kumamoto, Japan). hASCs were seeded at 1.0×10^4 cells per well on the five samples (50 nm, 70 nm, 100 nm, SLA, smooth surface Ti), respectively, in a 24-well plate. After 2, 4 and 24-h of cell culture, the medium was changed and the cells were incubated with the counting reagent for 3 h, according to the manufacturer's instructions. The relative cell number was determined by measuring light absorbance (OD) at a wavelength of 450 nm of the formazan dye product in the cultures [21]. Before SEM observation, samples were washed with phosphate buffered saline (PBS) and fixed overnight in cacodylate buffered 4% glutaraldehyde at 4 °C. The specimens were postfixed in 1% OsO$_4$ for 1.5 h, dehydrated with a graded series of ethanol, dried in a critical point dryer (Micro Modul YO-230, Thermo Scientific, Waltham, MA, USA), mounted onto aluminum stubs, sputter coated with gold, and viewed under a field emission SEM (FESEM, Hitachi, S4800, Japan) [22]. Before observation under a confocal microscope, samples were washed with PBS and fixed in 4% paraformaldehyde for 20 min at room temperature. Then samples were washed three times in PBS and subsequently postfixed in 0.1% Triton X-100 for 5 min at room temperature. The samples were then washed three times in PBS and incubated with fluorescein isothiocyanate (FITC)-labeled phalloidin for 25 min at 37 °C. Samples were washed and incubated in 5 μg/ml 6-diamidino-2-phenylindole (DAPI) solution for 10 min at 37 °C. Following three additional washings with PBS, samples were transferred to a glass slide with mounting medium, covered with a coverslip, and viewed under a Confocal Zeiss Axiovert 650 microscope (Carl Zeiss Microimaging, Oberkochen, Germany) using the laser with wavelengths of 488 nm (green, FITC-labeled phalloidin) and 405 nm (blue, DAPI). hASCs proliferation was also measured by CCK8 after 0, 1, 2, 3, 4, 5 and 6-day cell cultures on different samples. Protein adsorption assay were performed by culturing 100 μg/ml FITC-labeled bovine serum albumin (FITC-BSA, Sigma–Aldrich) for 30 min at 37 °C on the specimens [23]. Following three washings with PBS, samples were viewed under a confocal microscope using the laser with wavelengths of 488 nm (green).

2.5. Alkaline phosphatase (ALP) activity

hASCs were seeded in 24-well plates at the same density as above and divided into ten groups, including 50 nm, 70 nm, 100 nm, SLA, smooth Ti surface without OI and the same five samples with OI. ALP activity was determined on the 7th and 14th day of osteoinduction. ALP levels were normalized to the total protein content at the end of the experiment, as previously described [24].

2.6. Alizarin red S (AR-S) staining and mineralization assays

hASCs were seeded in 24-well plates and divided into ten groups as above. Mineralization was determined by staining with AR-S on days 14 and 21 after osteoinduction. To quantify matrix calcification, plates were washed three times with PBS and fixed with ethanol for 30min, and then stained with 0.5% AR-S in dH$_2$O (pH 4.0) for 1 h at RT. After staining, the samples were washed three times with dH$_2$O, followed by 70% ethanol. To quantify matrix mineralization, AR-S-stained samples were incubated in 100 mM cetylpyridinium chloride for 1 h to solubilize and release calcium-bound AR-S into the solution. The absorbance of the released AR-S was measured at 562 nm [25].

2.7. RNA extraction, reverse transcription, and quantitative real-time PCR

hASCs were seeded in 6-well plates and divided into ten groups as above. Total cellular RNAs were isolated on 7 and 14 days after osteoinduction using the Trizol reagent (Invitrogen, Carlsbad, CA, USA) and used for first strand cDNA synthesis with the Reverse Transcription System (Roche, Basel, Switzerland). Quantifications of all gene transcripts were performed by real-time polymerase chain reaction (qPCR) using a Power SYBR Green PCR Master Mix and an ABI PRISM 7500 sequence detection system (Applied Biosystems, Foster City, CA, USA). The expression of β-actin was detected as the internal control. The primers used were: Runx2, (forward) 5′-ATGGGATGGGTGTCTCCACA-3′ and (reverse) 5′-CCACGAAGGGGAACTTGTC-3′; OC, (forward) 5′-CACTCCTCGCCCTATTGGC-3′ and (reverse) 5′-CCCTCCTGCTTGGA-CACAAAG-3′; RBP2, (forward) 5′-GTCCAGCGCCTGAATGAACTT -3′ and (reverse) 5′-GCAACAATCTTGCTCAAAGCATA -3′; β-actin, (forward) 5′-CATGTACGTTGCTATC-CAGGC-3′, (reverse) 5′-CTCCTTAATGTCACGCACGAT-3′. The cycle threshold values (Ct values) were used to calculate the fold differences by the ΔΔCt method [19].

2.8. Immunofluorescence

The hASCs were seeded in 24-well plates and divided into ten groups as above. After 7 and 14-days of osteoinduction, samples were washed with PBS and fixed in 4% paraformaldehyde for 20 min at room temperature. The samples were washed three times in PBS and postfixed in 0.1% Triton X-100 for 15 min at room temperature. The samples were washed another three times in PBS and then incubated with 1:200 anti-osteocalcin primary antibodies (Santa Cruz, Dallas, TX, USA) overnight at 4 °C. Samples were washed and incubated in 1:500 anti-rabbit secondary antibodies (4412S, Cell Signaling Technology, Beverly, MA, USA) for 1 h at RT. The samples were washed and incubated in 5 μg/ml DAPI solution for 10 min at 37 °C. Following three additional washings with PBS, specimens were transferred to a glass slide with mounting medium, covered with a coverslip, and viewed under a Confocal Zeiss Axiovert 650 microscope using the laser with wavelengths of 488 nm (green, osteocalcin) and 405 nm (blue, DAPI). To examine the methylation of H3K4, 1:500 anti-tri-H3K4-methylation primary antibodies (Cell Signaling Technology) were incubated overnight. The incubation of the secondary antibody and DAPI was the same as above. DAPI was viewed at 405 nm but changed to red color in the photos because tri-methylation of H3K4 and DAPI both were located in the nucleus.

2.9. Ectopic bone formation in vivo

hASCs-coated TiO₂-nanotube disks were implanted into the back subcutaneous area of nude mice for in vivo study, referring to Hall et al.'s study design [26]. Implants were generally divided into four groups, including materials coated with hASCs cultured in osteoinducing medium (OI-ASC), materials without hASCs immersed in osteoinducing medium (OI-nASC), materials coated with hASCs cultured in proliferation medium (nOI-ASC) and materials immersed in proliferation medium (nOI-nASC). In each group, 50 nm, 70 nm and 100 nm nanotubes and positive control SLA were included to select the optimal dimension of TiO₂ nanotubes. After 7 days of in vitro culture, 8-week-old male BalB/c nude mice were anaesthetized with pentobarbital, and the above implants were placed aseptically into the dorsal subcutaneous area. At 4 and 8 weeks after surgery, the implants were harvested together with their surrounding tissues (10 implants for each group). The tissues were fixed by formalin, infiltrated by resin, and hard tissue slices were observed under light microscope after H.E. and toluidine blue staining.

2.10. Chromatin immunoprecipitation (ChIP) assay

The ChIP assay was performed as previously described [27]. Briefly, nonspecific rabbit IgG and H3K4me3 antibodies (all from Cell Signaling Technology) were incubated with Protein A beads (Novex by Life Technology, Grand Island, NY, USA) at 4 °C for 2 h. On the 7th and 14th day after osteoinduction, hASCs were cross-linked in 1% formaldehyde for 10 min and resuspended in 200 μl lysis buffer (1% sodium dodecyl sulfate [SDS], 10 mM EDTA, and 50 mM Tris—HCl [pH 8.0]). The nuclear lysates were sonicated and diluted 10-fold with immunoprecipitation buffer (0.5 mM EGTA, 140 mM NaCl, 10 mM Tris—HCl [pH 7.5], 1% Triton X-100, 0.1% SDS, 1 mM EDTA). The lysates were then immunoprecipitated with antibody—beads complexes for 12 h at 4 °C. After successive washings, immune complexes were delinked at 68 °C for 2 h. DNA was extracted by phenol—chloroform—isoamylalcohol (25:24:1) and the phenol was then eliminated by chloroform—isoamylalcohol (24:1). The precipitated DNA was amplified using real-time PCR. Primer pairs used in this study were as follows: Runx2 promoter, (forward) 5′-GGCTCCTTCAGCATTTG-TATTC-3′, (reverse) 5′-GCTCTTTCTCTCTCTCTCTTTCTC-3′; OC promoter, (forward) 5′-GTGGCTCACCCTCCATCAC-3′ and (reverse) 5′-CCTCCAGCACTGTTTATACCCT-3′.

2.11. Western blotting of RBP2 protein expression

After 7 and 14 days of osteoinduction, hASCs cultured on SLA and 70 nm nanotubes were resuspended in 200 μl lysis buffer, sonicated, and then centrifuged to obtain the supernatant. The Pierce BCA protein assay kit (Thermo Scientific) was used to measure the protein concentrations. Loading buffer was added to protein samples, which were boiled at 95 °C for 5 min. SDS-PAGE was performed and the proteins were transferred to polyvinylidene difluoride membranes. After blocking

by incubation in non-fat dried milk, the membrane was incubated with anti-RBP2 antibodies (1:1000, Cell Signaling Technology) overnight. The membrane was then incubated with the secondary antibody and developed using an ECL kit (CWBIO, Beijing, China) to visualize the immunoreactive protein bands.

2.12. RNA interference and lentiviral production and infection

Small interfering RNA (si-RNA) sequences targeting RBP2 (si-RNA: GCTGTAC-GAGAGTATACAC) were designed and cloned into the pLL3.7 shuttle vector, which contains an independent enhanced green fluorescent protein (EGFP) cassette. The recombinant construct and nonspecific si-RNA construct (control group) were then transiently transfected into HEK293T cells. The viral supernatants were collected 48 h later, clarified by filtration, and concentrated by ultracentrifugation. The concentrated viruses were used to infect hASCs [19]. The infected cells were then cultured on 70 nm nanotubes and SLA, with or without osteoinduction, and the differences in osteogenic differentiation between the knockdown group and control group were compared.

2.13. Statistics analysis

All data were analyzed among groups using one-way ANOVA plus the least significant difference procedure (LSD) test ($p < 0.05$). The ChIP assay was analyzed by a t test ($p < 0.05$) using SPSS 19.0 software (SPSS Inc., Chicago, IL, USA).

3. Results

3.1. Surface characterization

The morphology of TiO₂-nanotube-array thin films, formed on the surface of titanium substrate using anodic oxidation at different voltage (10 V, 20 V and 25 V) for 2 h and annealed at 450 °C for 2 h, was characterized by Scanning Electronic Microscopy (SEM) to observe the nanotubes geometric parameters (Fig. 1A). The outer diameters of the nanotubes were approximately 50 nm (10 V), 70 nm (20 V) and 100 nm (25 V) respectively. Atomic force microscope (AFM) demonstrated that the surface roughness (measuring by arithmetical mean deviation of the profile, Ra) of TiO₂ nanotubes increased as the diameter increased. The 70 nm and 100 nm TiO₂ nanotubes exhibited higher roughness compared with sandblasting with large grit and acid-etching (SLA) surface (Fig. 1B). The X-ray diffraction (XRD) patterns of the nanotube films demonstrated that unannealed anodized nanotubes showed only Ti peaks, similar to SLA and smooth Ti surfaces. However, anatase TiO₂ peaks were detected on the annealed specimens, indicating that the TiO₂ nanotube layers changed from amorphous structure to anatased TiO₂ through annealing at 450 °C for 2 h (Fig. 1C). Contact angle measurement showed that the contact angle decreased and the surface energy increased as the diameter increased; i.e., TiO₂ nanotubes with larger diameters had better hydrophilicity. All TiO₂ nanotubes were more hydrophilic than SLA and smooth Ti surfaces. Contact angles measured by simulated body fluid (SBF) demonstrated a similar tendency, and the contact angles were generally lower than in double distilled water (ddH₂O) (Fig. 1D).

3.2. hASCs adhesion and proliferation on TiO₂ nanotubes of different diameters

Using SEM (Fig. 2A), the morphology and fine structure, e.g. pseudopodia, of the adhered cells could be observed, while confocal microscopy photographs of FITC-Phalloidin staining (Fig. 2B) helped to view both the morphology and number of the adhered cells. Cell counting assay by cell-counting kit-8 (CCK8) provided a quantitative result for hASCs adhesion (Fig. 2C). After only 2 h of hASCs culture, cells extended obvious lamellipodia on all three groups of TiO₂ nanotube surfaces, and the number of adhered cells on nanotubes was higher than that on SLA and smooth titanium surfaces. In contrast, cells were generally round with only short pseudopodium on the SLA surface, while on smooth Ti surface, cells were round with no pseudopodium and the adhering
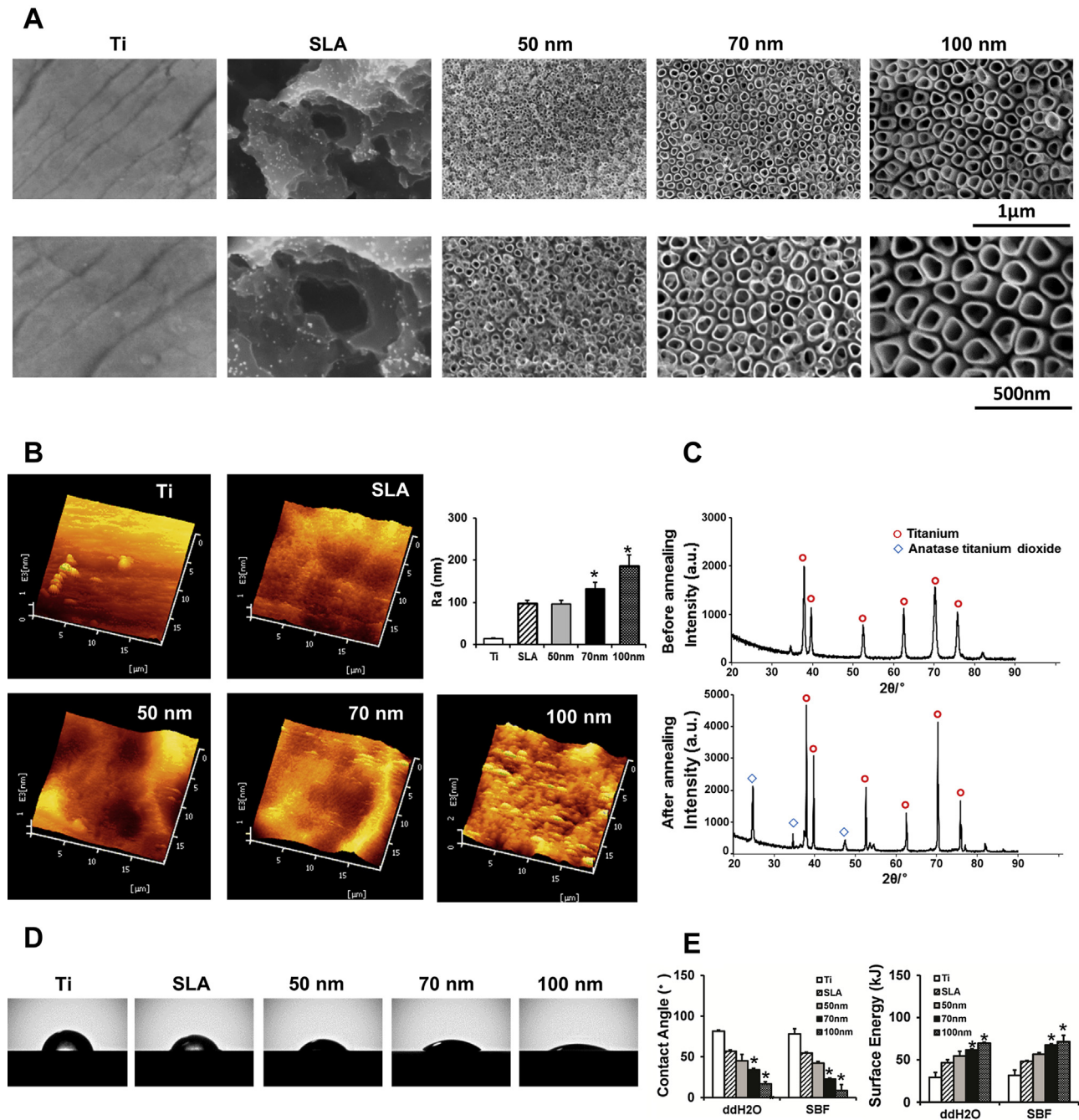
Fig. 1. Surface characterization of TiO₂ nanotubes. (A) Scanning electron microscopic observation (top view) of TiO₂ nanotubes with three different nanotube diameters, 50 nm, 70 nm and 100 nm, created by controlling anodizing potentials at 10 V, 20 V and 25 V at 50,000× and 100,000× magnification. (B) Atomic force microscopy (AFM) observation and roughness of TiO₂ nanotubes compared with sandblasting with large grit and acid-etching (SLA) and smooth titanium surface. (C) X-ray diffraction (XRD) patterns of TiO₂ nanotube arrays before and after heat treatment at 450 °C. (D) Photographs of contact angle measurement of water. (E) Contact angle and surface energy in water and simulated body fluid (SBF). *: compared with SLA, $p < 0.05$.

cells were the fewest. After 4 h of culture, even longer and net-like pseudopodia could be seen on all three groups of TiO₂ nanotube surfaces and the number of adhered cells was higher than on SLA and smooth titanium surfaces. On the SLA surface, the pseudopodia extended, but were obviously shorter than those on the nanotube groups. However, on the smooth titanium surface, cells remained round, with few pseudopodia. At 24 h of culture, cells had extended to a larger polygonal morphology on the nanotube surfaces, while spindle cells could be observed on SLA and smooth titanium surfaces. CCK8 assays demonstrated that at 2, 4 and 24 h after culture, there were more adherent hASCs on the TiO₂ nanotube surfaces

compared with SLA surface ($p < 0.05$). The number of cells on the 70 nm nanotubes was higher than that on the other groups ($p < 0.05$).

For hASCs proliferation, a logarithmic proliferation curve was observed on all surfaces, and there was no difference between the TiO₂ nanotubes and control surfaces over 0–4 days. On the 5th day, the proliferation on SLA and smooth surface reached a plateau; however, cells still continued to show a growth tendency on the surfaces of the TiO₂ nanotubes. The proliferation of hASCs on the nanotube surfaces reached a plateau on the 6th day of culture (Fig. 2D).
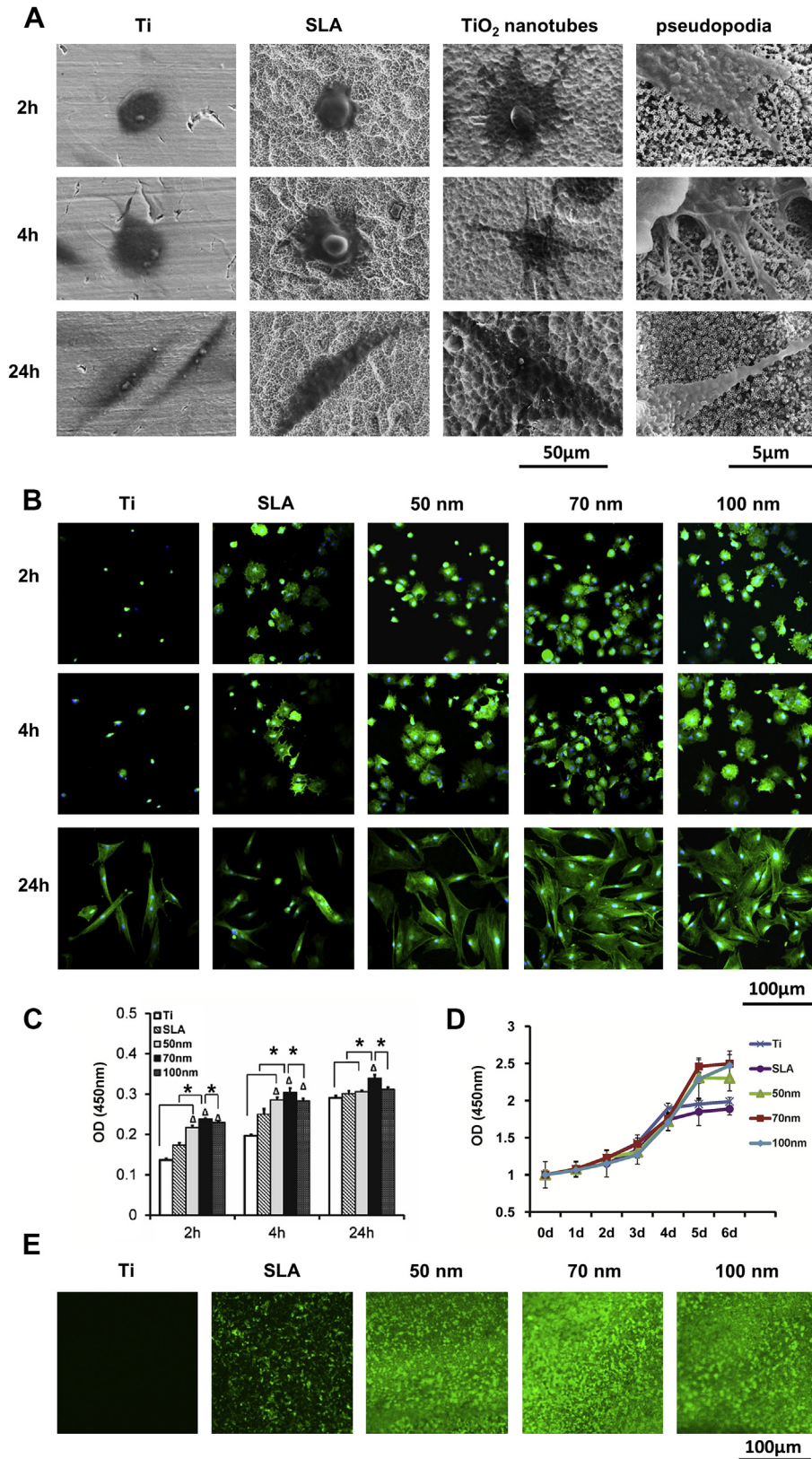
Fig. 2. Human adipose-derived stem cells (hASCs) adhesion and proliferation on TiO$_2$ nanotubes. (A) Scanning electron microscopic observation of hASCs on TiO$_2$ nanotubes, sandblasting with large grit and acid-etching (SLA) and smooth titanium surface after 2 h, 4 h and 24 h of culture at 1000× magnification. Pseudopodia of hASCs extending on TiO$_2$ nanotubes were observed at 10,000× magnification. (B) Confocal micrographs of hASCs on TiO$_2$ nanotubes with diameters of 50 nm, 70 nm and 100 nm, SLA and smooth titanium surface after 2 h, 4 h and 24 h of culture (100×). Phalloidin is colored green and nuclei are colored blue. (C) CCK8 assay of adhering hASCs on TiO$_2$ nanotubes, SLA and smooth titanium surface after 2 h, 4 h and 24 h of culture. (D) Growth curves of hASCs on TiO$_2$ nanotubes, SLA and smooth titanium surface. (E) Bovine serum albumin (BSA) adsorption on TiO$_2$ nanotubes, SLA and smooth titanium after 2 h of incubation. Δ: compared with SLA, $p < 0.05$; *: compared with 70 nm nanotubes, $p < 0.05$. (For interpretation of the references to color in this figure legend, the reader is referred to the web version of this article.)

3.3. BSA adsorption

After 2 h of incubation of FITC-BSA, samples were observed under a confocal immunofluorescence microscope. On TiO_2-nanotube surfaces, the green fluorescence was almost equally distributed, among which 70 nm nanotube layer showed the highest population of protein aggregates. For the SLA surface, BSA only attached to the prominent area of the surface, while green fluorescence was barely observed on the smooth titanium surface (Fig. 2E).

3.4. Osteogenic differentiation of hASCs on TiO_2 nanotubes with different diameters

After 7 days of osteoinduction (OI), the alkaline phosphatase (ALP) activity of 70 nm nanotubes with OI was higher than all other groups, including SLA ($p < 0.05$). The ALP activity of 70 nm nanotubes without OI was also higher than all other groups ($p < 0.05$). On the 14th day of OI, the tendency was the same as the 7th day, with more obvious osteogenic advantages of 70 nm nanotubes (Fig. 3A).

AR-S staining and mineralization assays demonstrated that after 14 days of OI, the AR-S stained specimens with OI showed that 70 nm nanotubes and 100 nm nanotubes had more obvious red staining than the others, and only on the surface of 70 nm nanotubes did sporadic calcium deposits nodules could be grossly observed. The AR-S stained specimens without OI showed that 70 nm and 100 nm specimens also had more obvious red staining than the others, with no calcium deposits nodule formation on any specimen. Mineralization assays demonstrated that the 70 nm group with OI was more mineralized than all other groups, including SLA ($p < 0.05$). As for groups without OI, the 70 nm specimen was also more mineralized than all other groups ($p < 0.05$). After 21 days of OI, increasing calcium nodule deposition could be seen on the 70 nm and 100 nm nanotube surfaces, with the 70 nm nanotube surfaces displaying more calcium deposition compared with 100 nm nanotubes. The AR-S stained specimens without OI showed that 70 nm and 100 nm specimens had more obvious red staining than others, and only on the surface of 70 nm nanotubes could sporadic calcium deposition nodules be observed. Mineralization assays demonstrated that the 70 nm specimen with OI was more mineralized than all other groups, including SLA ($p < 0.05$). As for groups without OI, the 70 nm specimen was also more mineralized than all other groups (Fig. 3B).

Gene expression of osteogenic-related genes Runx2 and osteocalcin (OC) were detected. After 7 days of OI, the relative Runx2 expression of hASCs on the surface of the 70 nm specimens both with and without OI was higher than on the SLA and smooth titanium surfaces ($p < 0.05$). After 14 days of OI, the relative Runx2 expression of the 70 nm specimen with OI was higher than that on the 50 nm nanotube, SLA and smooth titanium surfaces ($p < 0.05$). The relative Runx2 expression of the 70 nm specimen without OI was higher than that of the SLA and smooth titanium surfaces ($p < 0.05$) (Fig. 3C). For OC, after 7 days of OI, the 70 nm specimen showed higher expression than the smooth titanium surface ($p < 0.05$), both with and without OI. On the 14th day of OI, the gene expression of OC increased in all groups, among which 70 nm showed higher OC expression compared with SLA and smooth titanium surfaces ($p < 0.05$). For the groups without OI, the OC expression level was higher on the 70 nm specimen compared with the 100 nm specimen ($p < 0.05$) (Fig. 3C).

OC expression detected by immunofluorescence showed that after 7 days of OI, the 70 nm specimen with OI had the strongest OC-positive staining than the other groups. Among groups without OI, sporadic green fluorescence could be seen on the surface of the 70 nm specimen, and less green staining could be seen on the 100 nm and SLA specimens. After 14 days of OI, the OC-positive staining of the 70 nm specimen with OI was stronger, and the tendency was similar to day 7 (Fig. 3D).

3.5. Ectopic bone formation in vivo

After 4 weeks of implantation, hard tissue slices were observed under a light microscope after hematoxylin and eosin (HE) and toluidine blue staining. Implant surfaces coated with hASCs after 7 days of OI demonstrated obvious bone matrix formation on the 70 nm nanotube surfaces. HE stained the bone matrix as uniform acidophilic tissue, while the toluidine blue staining was uniformly dark blue with sporadic osteogenic-related cells. Only if bone tissue showed both HE staining and toluidine blue staining, did we consider it as actual bone formation. By contrast, fibrovascular tissue with large amounts of spindle-like cells could be observed on the surface of the SLA specimen. Interestingly, on the surface without hASCs, acidophilic tissue could also be observed on the surface of the 70 nm nanotube. Implant surfaces covered with hASCs without OI showed acidophilic bone tissue on the 70 nm nanotube surfaces, while fibrous tissue formed on the surface of the other groups (Fig. 4A).

After 8 weeks of implantation, ectopic bone formation was more significant on the surface of the 70 nm coated with hASCs with OI. The neo-bone layer reached a thickness of about 60 μm and the number of cells in the bone matrix decreased. Acidophilic tissue under HE staining and blue tissue under toluidine blue staining could be seen on the surface of the SLA specimen coated with hASCs with OI, but there was no obvious bone matrix formation. On the surface of 70 nm nanotubes immersed in OI medium without hASC, bone matrix formation could also be seen. As for implant surfaces covered with hASCs but without OI, ectopic bone formation was more obvious than at 4 weeks on the surface of the 70 nm nanotubes, while no bone formed on 70 nm nanotubes immersing in medium without OI (Fig. 4B).

3.6. Epigenetic regulation of TiO_2 nanotubes on hASCs

Examination of the tri-methylation level of H3K4 by immunofluorescence showed that after 7 and 14 days of OI, the 70 nm specimen with OI demonstrated the strongest green fluorescence than all other groups. The immunofluorescence of specimens without OI demonstrated a similar, but weaker, tendency compared with samples with OI (Fig. 5A). Chromatin Immunoprecipitation (ChIP) assays demonstrated that the tri-methylation of H3K4 at the promoter area of osteogenic genes, including Runx2 and OC, was significantly enhanced on the surface of the 70 nm specimen compared with the SLA specimen after 7 days of culture in osteogenic medium. On the 14th day of OI, the tri-methylation of H3K4 at the promoter area of Runx2 and OC on the surface of the 70 nm specimen was still higher than that of the SLA specimen, while the difference was less than that on the 7th day of OI (Fig. 5B).

After 7 days of osteoinduction, the relative RBP2 expression of the 70 nm specimen with OI was lower than the 50 nm, SLA and smooth titanium surface specimens ($p < 0.05$). The relative RBP2 expression of the 70 nm specimen without OI was the lowest among all groups ($p < 0.05$). After 14 days of OI, the expression of RBP2 decreased, and the relative RBP2 expression of the 70 nm specimen was lower than that of 50 nm, SLA and smooth titanium surface specimens ($p < 0.05$). The relative RBP2 expression of the 70 nm specimen without OI was lower than the SLA and smooth titanium surface specimens (Fig. 5C). RBP2 protein expression showed similar tendency to the gene expression; i.e., RBP2 was expressed at a lower level on 70 nm nanotubes compared with SLA specimens after 7 and 14 days of OI (Fig. 5D).
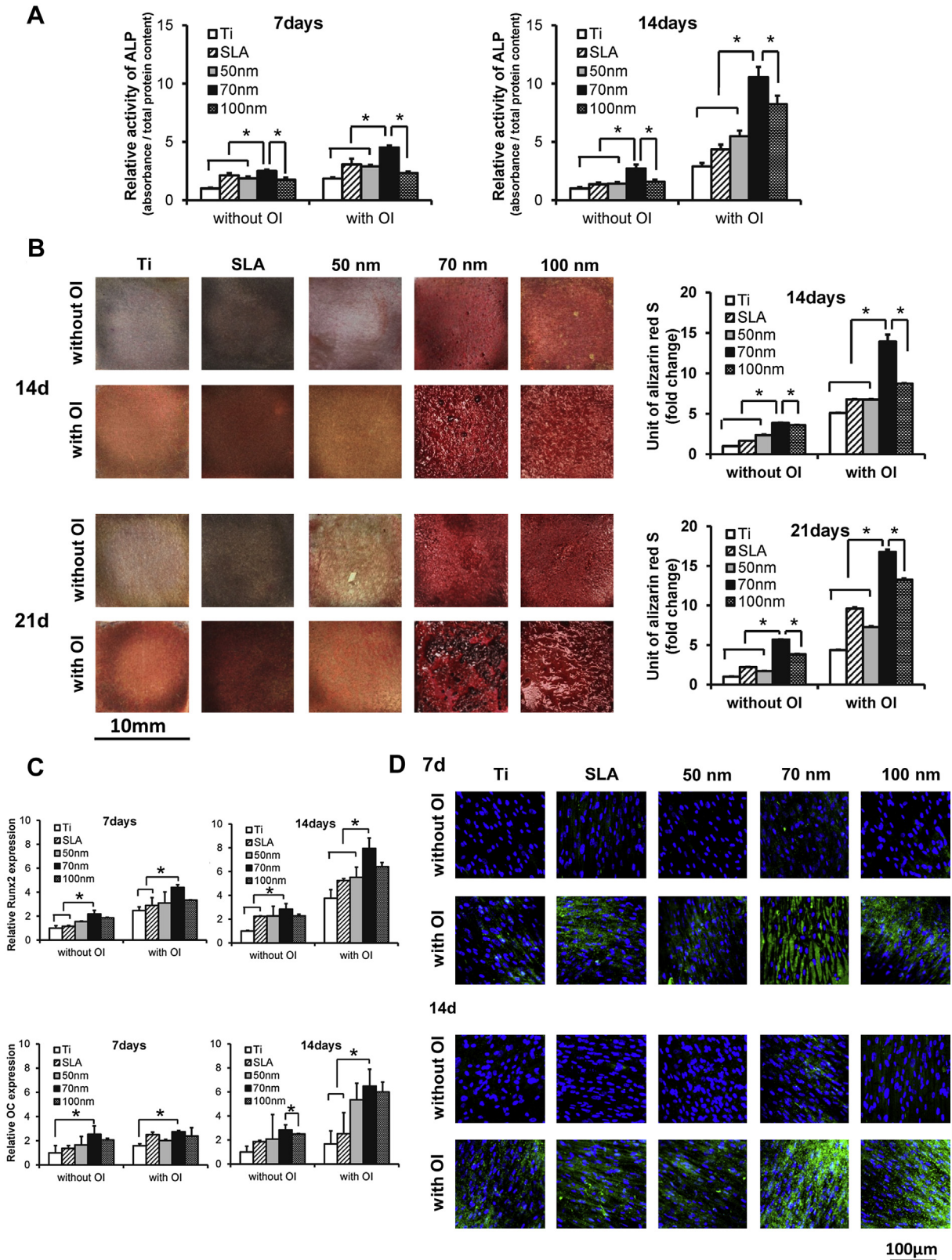
Fig. 3. Osteogenic differentiation of human adipose-derived stem cells (hASCs) on TiO$_2$ nanotubes *in vitro*. (A) Alkaline phosphatase (ALP) activity of hASCs cultured on TiO$_2$ nanotubes with diameters of 50 nm, 70 nm and 100 nm, SLA and smooth titanium surface for 7 and 14 days. (B) Alizarin Red staining and mineralization assay at 14 and 21 days. (C) The expression of osteogenic genes in hASCs cultured on different groups for 7 and 14 days. (D) Immunofluorescent staining for osteocalcin (OC) in hASCs cultured on different groups for 7 and 14 days (100×). OC is colored green and nuclei are colored blue.*$p < 0.05$. (For interpretation of the references to color in this figure legend, the reader is referred to the web version of this article.)
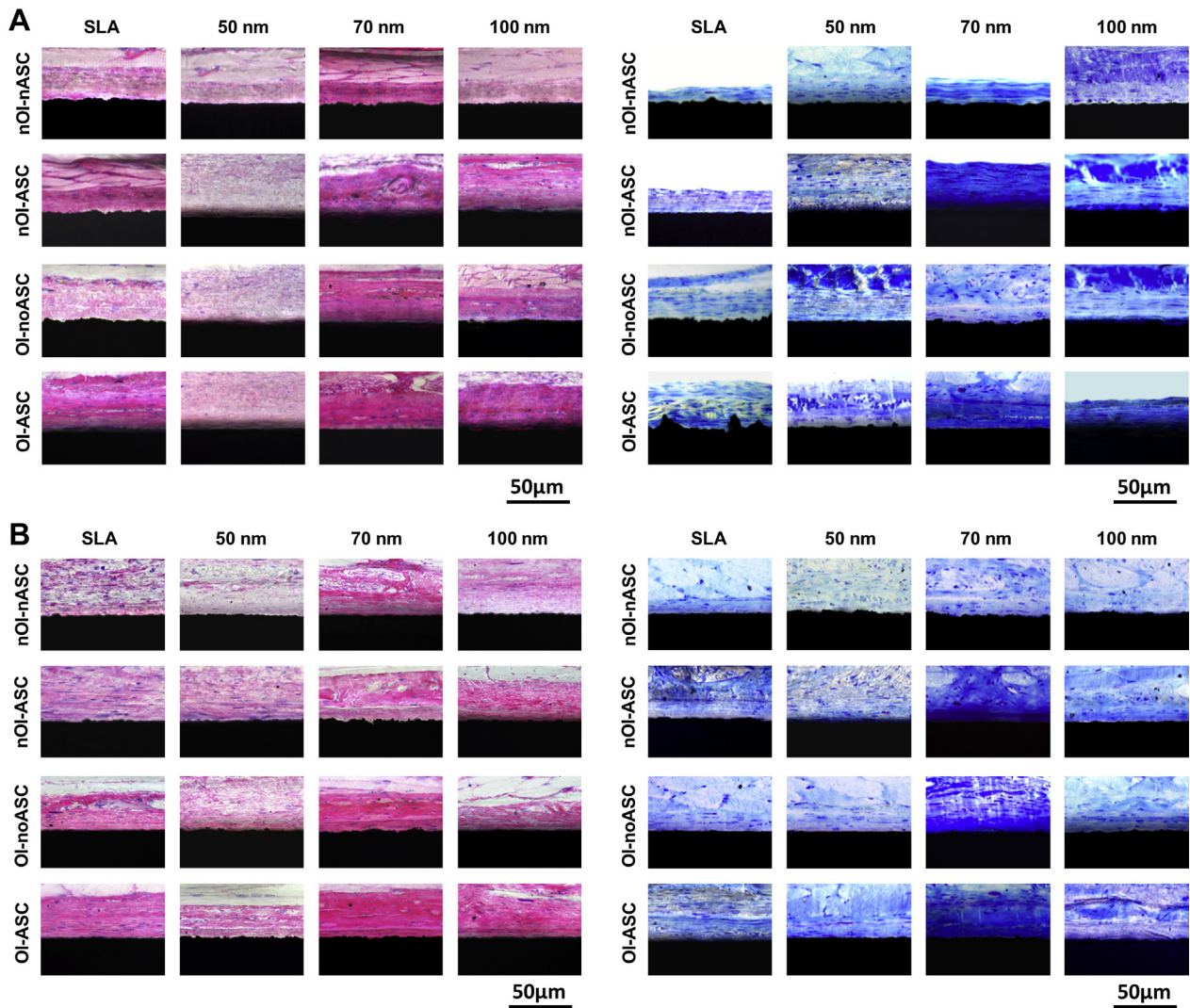
Fig. 4. Ectopic bone formation. (A) Hematoxylin and eosin (HE) and toluidine blue staining on the hard tissue slices after 4 weeks of implantation of TiO₂ nanotubes with diameters of 50 nm, 70 nm and 100 nm, SLA and smooth titanium specimens. (B) HE and toluidine blue staining on the hard tissue slices after 8 weeks of implantation (100 ×). nOI-nASC: without osteoinducing medium (OI), without human adipose derived stem cells (hASCs); nOI-ASC: without OI, with hASCs; OI-nASC: with OI, without hASCs; OI-ASC: with OI, with hASCs.

3.7. Osteogenic differentiation of RBP2-knockdown hASCs on TiO₂ nanotubes

hASCs were infected by a lentivirus expressing an *RBP2* short interfering RNA (si-RNA) and a control si-RNA and the transfection rate was more than 90% (Fig. 6A). RBP2 protein expression was confirmed by western blotting and showed a significant decrease in RBP2 expression in hASCs transfected by the *RBP2*-si-RNA (Fig. 6B).

ALP activity assays on the 7th day of OI demonstrated that *RBP2*-knockdown hASCs had higher ALP activity compared with control hASCs cultured on the same surface in the same medium ($p < 0.05$). Both *RBP2*-knockdown hASCs and control hASCs cultured on 70 nm nanotube surfaces showed higher ALP activities than the same cells cultured on the SLA surface ($p < 0.05$), and the difference between the 70 nm and SLA was even larger when *RBP2* was knocked down (Fig. 6C). After 14 days of OI, *RBP2*-knockdown hASCs on 70 nm nanotubes showed even higher ALP activity compared with SLA, demonstrating a significant difference for the control hASCs between 70 nm and SLA (Fig. 6C).

AR-S staining and mineralization assays demonstrated that after 14 days of OI, calcium deposition nodules could only be seen on the 70 nm specimens cultured with *RBP2*-knockdown hASCs and control hASCs. *RBP2*-knockdown hASCs demonstrated more calcium deposition nodules. Mineralization assays demonstrated that both *RBP2*-knockdown hASCs and control hASCs cultured on 70 nm nanotube surfaces more mineralized than the cells on the SLA specimen, and the difference between the 70 nm and SLA specimens was even larger when *RBP2* was knocked down. Control hASCs on 70 nm nanotubes even demonstrated higher mineralization levels than *RBP2*-knockdown hASCs on SLA (Fig. 6D). After 21 days of OI, even more and larger calcium deposition nodules could be observed on the 70 nm nanotubes cultured with *RBP2*-knockdown hASCs and control hASCs, and there was still more deposition on the 70 nm nanotubes with *RBP2*-knockdown hASCs. Mineralization assays demonstrated more obvious differences between the 70 nm and SLA surfaces cultured with *RBP2*-knockdown hASCs compared with control hASCs. Control hASCs on the 70 nm nanotubes showed even higher mineralization levels than *RBP2*-knockdown hASCs on SLA specimens compared with 14 days (Fig. 6D).
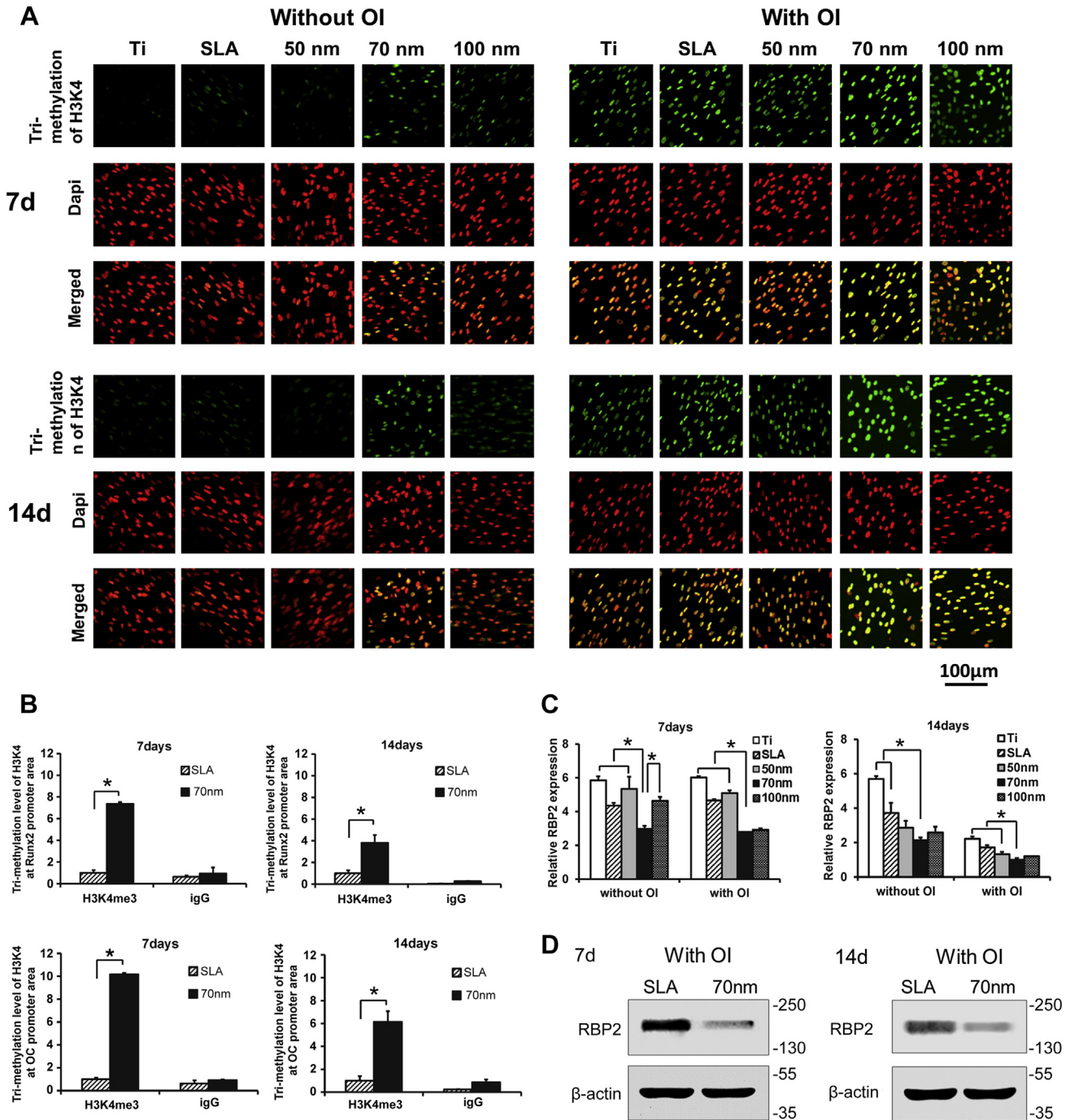
Fig. 5. Epigenetic regulation of TiO$_2$ nanotubes on human adipose derived stem cells (hASCs). (A) Immunofluorescent staining for tri-methylation of H3K4 in hASCs cultured on TiO$_2$ nanotubes with diameters of 50 nm, 70 nm and 100 nm, SLA and smooth titanium surface for 7 and 14 days. Tri-methylation of H3K4 is shown in green and nuclei are in red. (B) Chromatin immunoprecipitation (ChIP) assay of Tri-methylation level of H3K4 at the promoter area of osteogenic genes Runx2 and osteocalcin (OC). (C) Gene expression of demethylase RBP2 at day 7 and day 14 after osteoinduction. (D) Protein expression of demethylase RBP2 at day 7 and day 14 after osteoinduction. *$p < 0.05$. (For interpretation of the references to color in this figure legend, the reader is referred to the web version of this article.)

4. Discussion

4.1. The effects of TiO$_2$ nanotubes of different diameters on protein adsorption, hASCs adhesion and proliferation

Our study demonstrated that TiO$_2$ nanotubes demonstrated better protein adsorption abilities than SLA and smooth titanium surface (Fig. 2E). Studies have shown that protein aggregation is central to cell adhesion and extension. When a material is initially exposed in culture medium or body fluid, proteins begin to absorb on the surface within 1 s [1]. The proteins adsorbed on the material will bind with receptors on the cell membrane, leading to cell adhesion [1,14]. In fact, there are several characteristics of the material that influence protein adsorption, including surface roughness, surface energy/wettability, crystallinity, feature size or feature geometry, and other mechanical properties [1]. In our study, surface characterization demonstrated that the roughness and wettability of TiO$_2$ nanotubes increased with increasing tube
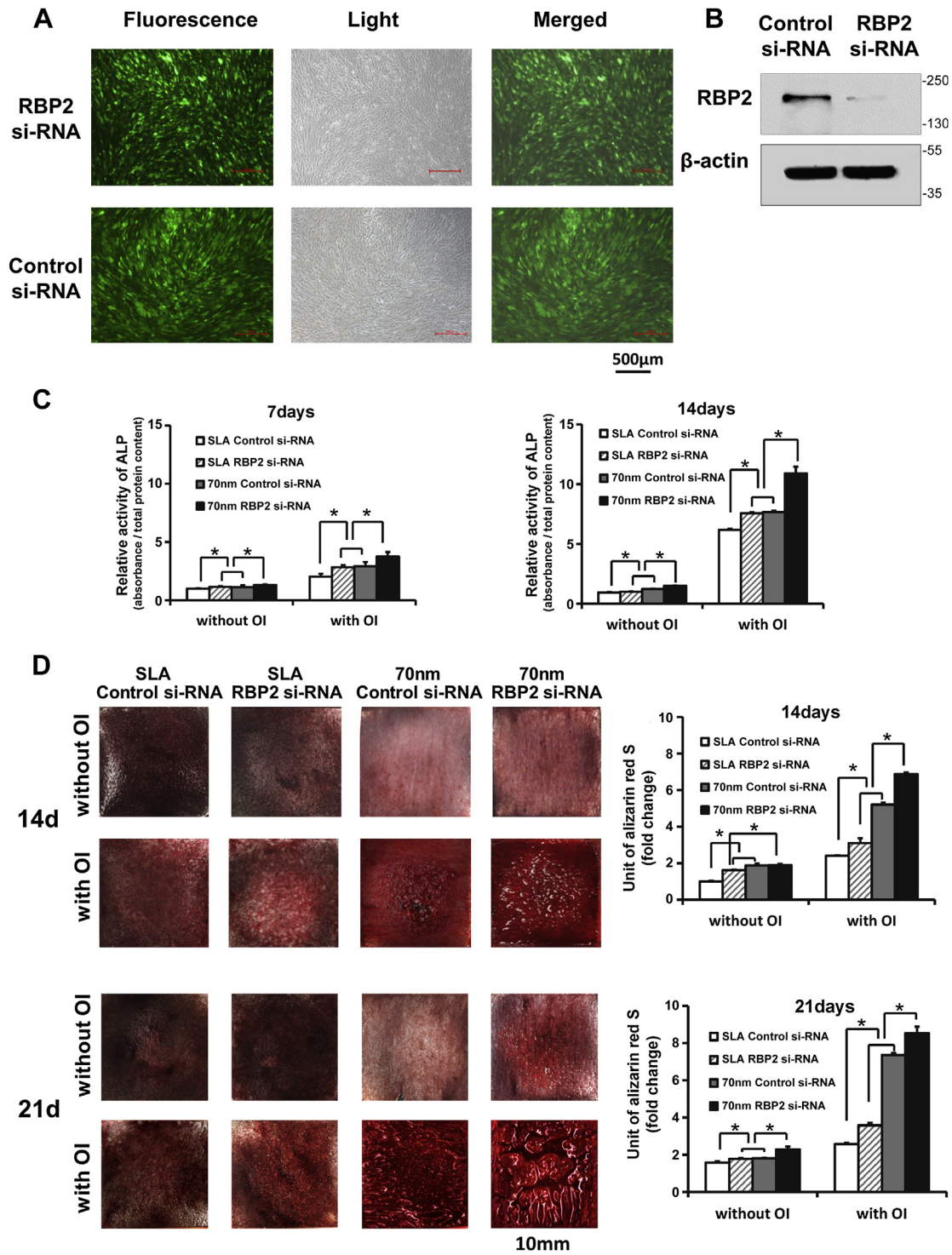
Fig. 6. Osteogenic differentiation of RBP2-knockdown human adipose-derived stem cells (hASCs) on TiO$_2$ nanotubes. (A) Fluorescence of hASCs after lentivirus transfection with RBP2 short interfering RNA (siRNA). (B) RBP2 expression of hASCs transfected with RBP2 si-RNA. (C) Alkaline phosphatase (ALP) activity of hASCs transfected with RBP2 si-RNA on sandblasting with large grit and acid-etching (SLA) and 70 nm nanotubes at day 7 and day 14 after osteoinduction. (D) Alizarin red S (AR-S) staining and mineralization assay of hASCs transfected with RBP2 si-RNA on SLA and 70 nm nanotubes at day 14 and day 21 after osteoinduction.*$p < 0.05$.

dimensions, and they were rougher and more hydrophilic than SLA and smooth titanium surfaces. However, we also noticed that the diameter of sandblasting grit was 110 μm, larger than the 20 μm × 20 μm scanning area of AFM, indicating that the deepest and the highest area of an SLA surface might not be detected simultaneously in the same scanning area, which might lead to

smaller result of roughness. In addition, anatase TiO$_2$ nanotubes surpassed rutile TiO$_2$ nanotubes in cell adhesion and differentiation [14,28,29]; thus, in our research, nanotube specimens were annealed under 450 °C to transform into the anatase form. In terms of tube diameters, proteins were likely to be trapped in tubes whose diameters were similar to their own dimensions, resulting in

a crowding effect that significantly reduces the mean protein—protein distance [14]. Based on the above factors that influence protein aggregation, an FITC-BSA adsorption assay demonstrated that proteins aggregated more and were almost equally distributed on TiO_2 nanotubes compared with SLA, where protein aggregated less and only adhered to the prominent area of the surface (Fig. 2E). Protein aggregation is the first step of cell adhesion; therefore pseudopodium could extend to a larger area under the help of dense proteins. Thus, the superior ability of protein adsorption may lead to faster cell adhesion on TiO_2 nanotubes.

We found that TiO_2 nanotubes could promote the adhesion of hASCs from the following three aspects: adhesion was obviously quicker compared with SLA and smooth titanium surfaces; more cells adhered to TiO_2 nanotubes than to SLA and smooth titanium surfaces because of the higher specific surface area of the TiO_2 nanotubes; cell spread extensively, with long pseudopodia, on the surface of TiO_2 nanotubes (Fig. 2A, B). Interestingly, we also found that 70 nm TiO_2 nanotubes had the best effect on cell adhesion compared with TiO_2 nanotubes with other diameters and SLA surfaces (Fig. 2C). In a previous study, Yu et al. [16] found no difference among the number of adhered MC3T3 cells on the surface of 20–70 nm nanotubes, while 100–120 nm nanotubes inhibited cell adhesion. These results were a little different to ours, which may result from different cell species and varied anodization process to form TiO_2 nanotubes.

For hASCs proliferation, TiO_2 nanotubes did not accelerate the rate of cell proliferation, but seemed to delay the emergence of the plateau phase, thus increasing the cell number at maximal confluence (Fig. 2D). This may have resulted from the enlarged specific surface area of its characteristic topography. Some previous studies also discussed the effect of TiO_2 nanotubes with different diameters on the proliferation of cells; however, the observation time was relatively limited, with no proliferation curve provided [12,14,16,30].

4.2. The effects of TiO_2 nanotubes on the osteogenic differentiation of hASCs

We found that 70 nm was the optimal dimension for the osteogenic differentiation of hASCs, and osteoinducing superiority of 70 nm nanotubes was more prominent when accompanied by osteogenic inducers, which was corroborated by a series of osteogenic indexes at different time points, including early osteogenic transcription factor Runx2, middle-period osteogenesis-related enzyme ALP, middle-and-late-period osteogenic marker OC, and late period osteogenesis assay AR-S (Fig. 3). Previous studies did not obtain a consistent result on the optimal dimension of nanotubes. Their viewpoints could be divided into three groups. The first one was that the osteogenic ability decreased with as the diameter of the nanotubes increased; that is, a small diameter was the optimal dimension. Park et al. [12,31] held the view that 15 nm could not only promote the osteogenic differentiation of rat BMMSCs, but could also promote the osteogenic differentiation of human pre-osteoblasts and the osteoclast differentiation of hematopoietic stem cells to accelerate bone remodeling. The second viewpoint was that the osteoinductive ability of nanotubes increased as the diameter increased; that is, a large diameter was the optimal dimension. Oh et al. [14] and Brammer et al. [15] found that 100 nm was the optimal dimension for the osteogenic differentiation of human BMMSCs and mouse MC3T3, respectively, which might be induced by the change of cytoskeletal stress caused by elongation of cells on larger diameter nanotubes. The third viewpoint was that a medium-sized diameter was the optimal dimension for osteogenic differentiation. Yu et al. [16] found that 70 nm was the optimal dimension for the osteogenic differentiation of mouse

MC3T3 cells. These divergent opinions may have resulted from the variations in cell type and/or cell species, as well as disparities in nanoscale features and physical properties of the nanotubes, such as the length of nanotubes, thickness of the nanotube walls and their crystal form. More importantly, the optimal dimension of TiO_2 nanotubes for bone tissue regeneration *in vivo* has not been fully demonstrated because of the lack of *in vivo* studies. Hence, to select the optimal surface morphology of TiO_2 nanotubes for clinical use, it is essential to translate the *in vitro* results into *in vivo* experiment based on human cells.

Therefore, in this study we implanted hASCs-coated TiO_2-nanotube disks into the back subcutaneous area of nude mice for *in vivo* study [26]. Implants were divided into four groups, including materials coated with hASCs cultured in osteoinductive medium, materials without hASCs immersing in osteoinductive medium, materials coated with hASCs cultured in proliferation medium and materials immersing in proliferation medium, to analyze whether TiO_2 nanotubes had an active osteoinductive ability, and whether it could adsorb osteoinducing factors. In each group, 50 nm, 70 nm and 100 nm nanotubes and positive control SLA were included to select the optimal dimension of TiO_2 nanotubes. To maintain the integrity of the nanotube and the surrounding tissue, we chose hard tissue slices for histological observation, avoiding the separation of the titanium specimen and the surrounding tissue for decalcification and routine histological slicing. HE and toluidine blue staining were used to analyze the newly formed tissue around the titanium specimen comprehensively. In HE staining, bone matrix is stained as uniform acidophilic tissue, with sporadic osteogenesis-related cells around it, while in toluidine blue staining, bone matrix showed as uniform dark blue staining and the osteogenesis-related cells were also stained as dark blue [32]. Only if bone tissue could be seen in both HE staining and toluidine blue staining, did we considered it as new bone formation. We found that after 4 and 8 weeks of implantation, 70 nm nanotubes coated with hASCs with OI showed the best neo-bone formation ability compared with all other groups. Meanwhile, new bone formation could also be observed around 70 nm nanotubes coated with hASCs without OI (Fig. 4). These results indicated a certain active osteoinducing ability of 70 nm nanotubes on hASCs. There were no obvious bone formation around 70-nm-nanotube implant without hASCs immersed in osteoinducing medium at 4 weeks, but sporadic bone matrix formation could be observed at 8 weeks, which was better than the 70 nm group immersed in proliferation medium. This indicated a certain adsorptive ability for osteoinducing factors of 70 nm nanotubes, thus promoting the osteogenic differentiation of autologous cells.

Recently, many researchers have studied the surface modification and drug delivery of TiO_2 nanotubes to enhance their osteoinducing ability. Lee et al. [33] found that N-acetyl cysteine-loaded TiO_2 nanotubes could reduce inflammatory responses around implants, thus enhancing osseointegration. Lai et al. [34] delivered BMP2 into TiO_2 nanotubes to enhance their osteoinducing ability. However, surface modification and drug delivery require the enrichment of autologous cells in the first place, which leads to osteogenic differentiation of autologous preosteoblasts and stem cells. Therefore, autologous-stem-cell-coated scaffolds or implants will become the trend for future clinical application, whose advantages are the acquisition of cell enrichment in advance and the induction of the process of osseointegration immediately after implantation [35]. On the selection of autologous stem cells, although BMMSCs have a better osteogenic differentiation ability, the inconvenience of gathering BMMSCs, the increased suffering of patients and limited cell numbers have impeded their clinical application. hASCs, on the other hand, are one of the most promising seed cells for bone tissue engineering, and have the

superiority of good accessibility, higher safety and full abundance compared with BMMSCs [36]. In spite of hASCs' preponderance in clinical transformation, their osteogenic potential compared with BMMSCs remains controversial [37–40]. Conventional approaches based purely on soluble factors to promote osteogenic differentiation of hASCs have resulted in limited success because of its transient effective time and unstable change to cell differentiation [41–43]. Hence, if a surface geometry could be discovered to elevate the osteogenic ability of hASCs quickly and stably, it would be an important breakthrough for both nanomedicine and the clinical translation of bone tissue engineering.

4.3. How does nanotopography promote osteogenic differentiation of hASCs?

Park [12] found that the expression of paxillin and β-integrin increased on rat BMMSCs when cultured on 15 nm nanotubes, suggesting that 15 nm was the optimal dimension, probably because 15 nm was similar with the adhesion interval of integrin. The aggregation of integrin led to the phosphorylation of FAK. Those reporting that a larger diameter was the optimal dimension explained this phenomenon through elongation of cells, which would cause changes of cytoskeletal stress [14,15]. However, until now, a more central and stable mechanism seems to have been neglected; i.e., epigenetic regulation, under which condition gene expression is regulated by the change in histone modification that does not change the DNA sequence [44–46]. So, does nanogeometry influence the osteogenic differentiation of stem cells through epigenetic regulation?

Our previous study [19] discovered that RBP2, a histone demethylase of H3K4, could inhibit the osteogenic differentiation of hASCs, depending on its demethylation activity to inhibit the gene expression of osteogenesis-associated genes. In this study, we discovered that TiO$_2$ nanotubes could inhibit the expression of RBP2 (Fig. 5C, D) and thus enhance the methylation level of H3K4 at the promoter regions of osteogenesis-associated genes, such as Runx2 and OC (Fig. 5A, B). It is reasonable to speculate that RBP2, and the other possible repression complexes, dissociate when stem cells are osteogenetically induced by nanogeometry and other osteoinduction conditions, and promoters of osteogenic genes become more accessible and are occupied by activation complexes involving histone methylation, such as H3K4 methylation. Thus, the chromatin is altered from a repressed to an active state, which switches on the osteogenic process [19]. In this study, a ChIP assay (Fig. 5B) was performed on two representative specimen groups, SLA and 70 nm nanotubes with OI, because it was not feasible to detect the methylation condition of 10 groups: a ChIP assay requires several control groups, including inter-group control (SLA and 70 nm), inner-group control (Input) and blank control (IgG) [27]. Furthermore, two kinds of cells, *RBP2*-knockdown hASCs and control hASCs, were used to confirm the role of RBP2 on the osteogenic differentiation promoted by nanogeometry, such as TiO$_2$ nanotubes. We found that 70 nm TiO$_2$ nanotubes showed significantly better osteoinducing ability compared with the SLA surface, and the difference between 70 nm nanotubes and SLA surface of *RBP2*-knockdown hASCs was larger than control hASCs, which may be caused by a synergistic inhibitory effect of both si-RNA and 70 nm nanotubes on *RBP2* expression (Fig. 6C, D). Therefore, we concluded that the 70 nm TiO$_2$ nanotubes promoted the osteogenic differentiation of hASCs through inhibition of *RBP2* expression. Other researchers [45,47–50] have reported that different histone modification sites, such as the methylation and acetylation of H3K9 and H3K27, influenced the osteogenic differentiation of stem cells, leading us to speculate that the epigenetic regulation of stem cell linage commitment was extensive and complex. Thus, more studies

and explorations are urgently expected to reveal the epigenetic regulation of how surface topography directs stem cell fate. Moreover, epigenetics is central to cellular differentiation and stem cell lineage commitment. A better understanding of the epigenetic mechanism of how geometric cues influence stem cells could improve bone tissue engineering and provide new insights into the modulation of surface modification and stem cell therapy. However, there were some limitations in this study. *In situ* bone defect models should be used and more *in vivo* investigations are essential before the clinical application of nanomaterials. Meanwhile, other mechanisms that we did not discover in this investigation might affect cellular differentiation and stem cell linage commitment. Therefore, further investigations are needed to aid the future application of nanomaterials to promote osteogenic differentiation of stem cells through epigenetic regulation.

5. Conclusions

Nanoscale geometry can influence cell differentiation, and 70 nm TiO$_2$ nanotubes are optimal for the osteogenic differentiation of hASCs, as compared with 50 nm and 100 nm, and are better than SLA both *in vitro* and *in vivo*. Nanoscale geometry can regulate the osteogenic differentiation of hASCs via an epigenetic mechanism: the appropriate nanotopography can upregulate the methylation level of H3K4 at the promoter regions of osteogenesis-associated genes by inhibiting of RBP2 expression.

References

[1] Brammer KS, Frandsen CJ, Jin S. TiO$_2$ nanotubes for bone regeneration. Trends Biotechnol 2012;30:315–22.
[2] Bettinger CJ, Langer R, Borenstein JT. Engineering substrate topography at the micro- and nanoscale to control cell function. Angew Chem Int Ed Engl 2009;48:5406–15.
[3] Clair S, Variola F, Kondratenko M, Jedrzejowski P, Nanci A, Rosei F, et al. Self-assembled monolayer of alkanephosphoric acid on nanotextured Ti. J Chem Phys 2008;128:144705.
[4] Dalby MJ, McCloy D, Robertson M, Wilkinson CD, Oreffo RO. Osteoprogenitor response to defined topographies with nanoscale depths. Biomaterials 2006;27:1306–15.
[5] Dalby MJ, Gadegaard N, Tare R, Andar A, Riehle MO, Herzyk P, et al. The control of human mesenchymal cell differentiation using nanoscale symmetry and disorder. Nat Mater 2007;6:997–1003.
[6] Dalby MJ, Hart A, Yarwood SJ. The effect of the RACK1 signalling protein on the regulation of cell adhesion and cell contact guidance on nanometric grooves. Biomaterials 2008;29:282–9.
[7] You MH, Kwak MK, Kim DH, Kim K, Levchenko A, Kim DY, et al. Synergistically enhanced osteogenic differentiation of human mesenchymal stem cells by culture on nanostructured surfaces with induction media. Biomacromolecules 2010;11:1856–62.
[8] Liu W, Wei Y, Zhang X, Xu M, Yang X, Deng X. Lower extent but similar rhythm of osteogenic behavior in hBMSCs cultured on nanofibrous scaffolds versus induced with osteogenic supplement. ACS Nano 2013;7:6928–38.
[9] Hosseinkhani H, Hosseinkhani M, Tian F, Kobayashi H, Tabata Y. Osteogenic differentiation of mesenchymal stem cells in self-assembled peptide-amphiphile nanofibers. Biomaterials 2006;27:4079–86.
[10] Moroni L, Licht R, de Boer J, de Wijn JR, van Blitterswijk CA. Fiber diameter and texture of electrospun PEOT/PBT scaffolds influence human mesenchymal stem cell proliferation and morphology, and the release of incorporated compounds. Biomaterials 2006;27:4911–22.

[11] Pozio A, Palmieri A, Girardi A, Cura F, Carinci F. Titanium nanotubes stimulate osteoblast differentiation of stem cells from pulp and adipose tissue. Dent Res J (Isfahan) 2012;9:S169–74.

[12] Park J, Bauer S, von der Mark K, Schmuki P. Nanosize and vitality: TiO₂ nanotube diameter directs cell fate. Nano Lett 2007;7:1686–91.

[13] Bauer S, Park J, Faltenbacher J, Berger S, von der Mark K, Schmuki P. Size selective behavior of mesenchymal stem cells on ZrO(2) and TiO(2) nanotube arrays. Integr Biol (Camb) 2009;1:525–32.

[14] Oh S, Brammer KS, Li YS, Teng D, Engler AJ, Chien S, et al. Stem cell fate dictated solely by altered nanotube dimension. Proc Natl Acad Sci U S A 2009;106:2130–5.

[15] Brammer KS, Oh S, Cobb CJ, Bjursten LM, van der Heyde H, Jin S. Improved bone-forming functionality on diameter-controlled TiO(2) nanotube surface. Acta Biomater 2009;5:3215–23.

[16] Yu WQ, Jiang XQ, Zhang FQ, Xu L. The effect of anatase TiO₂ nanotube layers on MC3T3-E1 preosteoblast adhesion, proliferation, and differentiation. J Biomed Mater Res A 2010;94:1012–22.

[17] Wang N, Li H, Lu W, Li J, Wang J, Zhang Z, et al. Effects of TiO₂ nanotubes with different diameters on gene expression and osseointegration of implants in minipigs. Biomaterials 2011;32:6900–11.

[18] Arnsdorf EJ, Tummala P, Castillo AB, Zhang F, Jacobs CR. The epigenetic mechanism of mechanically induced osteogenic differentiation. J Biomech 2010;43:2881–6.

[19] Ge W, Shi L, Zhou Y, Liu Y, Ma GE, Jiang Y, et al. Inhibition of osteogenic differentiation of human adipose-derived stromal cells by retinoblastoma binding protein 2 repression of RUNX2-activated transcription. Stem Cells 2011;29:1112–25.

[20] Li S, Ni J, Liu X, Zhang X, Yin S, Rong M, et al. Surface characteristics and biocompatibility of sandblasted and acid-etched titanium surface modified by ultraviolet irradiation: an in vitro study. J Biomed Mater Res B Appl Biomater 2012;100:1587–98.

[21] Liu YS, Ou ME, Liu H, Gu M, Lv LW, Fan C, et al. The effect of simvastatin on chemotactic capability of SDF-1alpha and the promotion of bone regeneration. Biomaterials 2014;35:4489–98.

[22] Liu Y, Zhang X, Liu Y, Jin X, Fan C, Ye H, et al. Bi-functionalization of a calcium phosphate-coated titanium surface with slow-release simvastatin and metronidazole to provide antibacterial activities and pro-osteodifferentiation capabilities. PLoS One 2014;9:e97741.

[23] Pegueroles M, Tonda-Turo C, Planell JA, Gil FJ, Aparicio C. Adsorption of fibronectin, fibrinogen, and albumin on TiO₂: time-resolved kinetics, structural changes, and competition study. Biointerphases 2012;7:48.

[24] Liu Y, Zhao Y, Zhang X, Chen T, Zhao X, Ma GE, et al. Flow cytometric cell sorting and in vitro pre-osteoinduction are not requirements for in vivo bone formation by human adipose-derived stromal cells. PLoS One 2013;8:e56002.

[25] Ge W, Liu Y, Chen T, Zhang X, Lv L, Jin C, et al. The epigenetic promotion of osteogenic differentiation of human adipose-derived stem cells by the genetic and chemical blockade of histone demethylase LSD1. Biomaterials 2014;35:6015–25.

[26] Hall J, Sorensen RG, Wozney JM, Wikesjo UM. Bone formation at rhBMP-2-coated titanium implants in the rat ectopic model. J Clin Periodontol 2007;34:444–51.

[27] Dahl JA, Collas P. A rapid micro chromatin immunoprecipitation assay (microChIP). Nat Protoc 2008;3:1032–45.

[28] Neupane MP, Park IS, Lee MH, Bae TS, Watari F. Influence of heat treatment on morphological changes of nano-structured titanium oxide formed by anodic oxidation of titanium in acidic fluoride solution. Biomed Mater Eng 2009;19:77–83.

[29] He J, Zhou W, Zhou X, Zhong X, Zhang X, Wan P, et al. The anatase phase of nanotopography titania plays an important role on osteoblast cell morphology and proliferation. J Mater Sci Mater Med 2008;19:3465–72.

[30] Yu WQ, Jiang XQ, Xu L, Zhao YF, Zhang FQ, Cao X. Osteogenic gene expression of canine bone marrow stromal cell and bacterial adhesion on titanium with different nanotubes. J Biomed Mater Res B Appl Biomater 2011;99:207–16.

[31] Park J, Bauer S, Schlegel KA, Neukam FW, von der Mark K, Schmuki P. TiO₂ nanotube surfaces: 15 nm – an optimal length scale of surface topography for cell adhesion and differentiation. Small 2009;5:666–71.

[32] Oliveira JM, Kotobuki N, Tadokoro M, Hirose M, Mano JF, Reis RL, et al. Ex vivo culturing of stromal cells with dexamethasone-loaded carboxymethylchitosan/poly(amidoamine) dendrimer nanoparticles promotes ectopic bone formation. Bone 2010;46:1424–35.

[33] Lee YH, Bhattarai G, Park IS, Kim GR, Kim GE, Lee MH, et al. Bone regeneration around N-acetyl cysteine-loaded nanotube titanium dental implant in rat mandible. Biomaterials 2013;34:10199–208.

[34] Lai M, Cai K, Zhao L, Chen X, Hou Y, Yang Z. Surface functionalization of TiO₂ nanotubes with bone morphogenetic protein 2 and its synergistic effect on the differentiation of mesenchymal stem cells. Biomacromolecules 2011;12:1097–105.

[35] Yu M, Zhou W, Song Y, Yu F, Li D, Na S, et al. Development of mesenchymal stem cell-implant complexes by cultured cells sheet enhances osseointegration in type 2 diabetic rat model. Bone 2011;49:387–94.

[36] Liu Y, Zhou Y, Feng H, Ma GE, Ni Y. Injectable tissue-engineered bone composed of human adipose-derived stromal cells and platelet-rich plasma. Biomaterials 2008;29:3338–45.

[37] Zhang W, Zhang X, Wang S, Xu L, Zhang M, Wang G, et al. Comparison of the use of adipose tissue-derived and bone marrow-derived stem cells for rapid bone regeneration. J Dent Res 2013;92:1136–41.

[38] Takemitsu H, Zhao D, Yamamoto I, Harada Y, Michishita M, Arai T. Comparison of bone marrow and adipose tissue-derived canine mesenchymal stem cells. BMC Vet Res 2012;8:150.

[39] Kang BJ, Ryu HH, Park SS, Koyama Y, Kikuchi M, Woo HM, et al. Comparing the osteogenic potential of canine mesenchymal stem cells derived from adipose tissues, bone marrow, umbilical cord blood, and Wharton's jelly for treating bone defects. J Vet Sci 2012;13:299–310.

[40] Hayashi O, Katsube Y, Hirose M, Ohgushi H, Ito H. Comparison of osteogenic ability of rat mesenchymal stem cells from bone marrow, periosteum, and adipose tissue. Calcif Tissue Int 2008;82:238–47.

[41] Gulati K, Aw MS, Findlay D, Losic D. Local drug delivery to the bone by drug-releasing implants: perspectives of nano-engineered titania nanotube arrays. Ther Deliv 2012;3:857–73.

[42] Hulsart-Billstrom G, Yuen PK, Marsell R, Hilborn J, Larsson S, Ossipov D. Bisphosphonate-linked hyaluronic acid hydrogel sequesters and enzymatically releases active bone morphogenetic protein-2 for induction of osteogenic differentiation. Biomacromolecules 2013;14:3055–63.

[43] Wang H, Zou Q, Boerman OC, Nijhuis AW, Jansen JA, Li Y, et al. Combined delivery of BMP-2 and bFGF from nanostructured colloidal gelatin gels and its effect on bone regeneration in vivo. J Control Rel 2013;166:172–81.

[44] Garcia-Bassets I, Kwon YS, Telese F, Prefontaine GG, Hutt KR, Cheng CS, et al. Histone methylation-dependent mechanisms impose ligand dependency for gene activation by nuclear receptors. Cell 2007;128:505–18.

[45] Ye L, Fan Z, Yu B, Chang J, Al HK, Zhou X, et al. Histone demethylases KDM4B and KDM6B promotes osteogenic differentiation of human MSCs. Cell Stem Cell 2012;11:50–61.

[46] Barkhordarian A, Sison J, Cayabyab R, Mahanian N, Chiappelli F. Epigenetic regulation of osteogenesis: human embryonic palatal mesenchymal cells. Bioinformation 2010;5:278–81.

[47] Tan J, Huang H, Huang W, Li L, Guo J, Huang B, et al. The genomic landscapes of histone H3-Lys9 modifications of gene promoter regions and expression profiles in human bone marrow mesenchymal stem cells. J Genet Genomics 2008;35:585–93.

[48] Teven CM, Liu X, Hu N, Tang N, Kim SH, Huang E, et al. Epigenetic regulation of mesenchymal stem cells: a focus on osteogenic and adipogenic differentiation. Stem Cells Int 2011;2011:201371.

[49] Du J, Ma Y, Ma P, Wang S, Fan Z. Demethylation of epiregulin gene by histone demethylase FBXL11 and BCL6 corepressor inhibits osteo/dentinogenic differentiation. Stem Cells 2013;31:126–36.

[50] Noer A, Lindeman LC, Collas P. Histone H3 modifications associated with differentiation and long-term culture of mesenchymal adipose stem cells. Stem Cells Dev 2009;18:725–36.